



Cite this: *J. Mater. Chem. C*,  
2024, 12, 4682

## Novel valleytronic and piezoelectric properties coexisting in Janus $\text{MoAZ}_3\text{H}$ ( $\text{A} = \text{Si}$ , or $\text{Ge}$ ; $\text{Z} = \text{N}$ , $\text{P}$ , or $\text{As}$ ) monolayers<sup>†</sup>

Xiaolin Cai, <sup>\*a</sup> Guoxing Chen,<sup>a</sup> Rui Li,<sup>a</sup> Zhixiang Pan<sup>a</sup> and Yu Jia <sup>\*bc</sup>

In this paper, for the newly proposed two-dimensional (2D) Janus  $\text{MoAZ}_3\text{H}$  ( $\text{A} = \text{Si}$ , or  $\text{Ge}$ ;  $\text{Z} = \text{N}$ ,  $\text{P}$ , or  $\text{As}$ ) monolayer (ML) materials, we theoretically explore the valleytronic and piezoelectric properties using first-principles calculations. The calculated results show that Janus  $\text{MoAZ}_3\text{H}$  MLs have obvious valleytronic properties due to the broken inversion symmetry and strong spin-orbit coupling (SOC) effects, and the spin-valley coupling of  $\text{MoAZ}_3\text{H}$  MLs can be enhanced from 173 to 283 meV by changing the  $\text{A}$  or  $\text{Z}$  element, comparable to the corresponding  $\text{MoA}_2\text{Z}_4$  MLs. The non-zero Berry curvatures with opposite signs at the  $K$  and  $K'$  points can induce the valley Hall effect. Furthermore, Janus  $\text{MoAZ}_3\text{H}$  MLs exhibit obvious in-plane and out-of-plane piezoelectric responses, and their independent  $d_{11}$  and  $d_{31}$  piezoelectric coefficients range from 1.62 to 8.60 pm V<sup>-1</sup> and from 0.058 to 0.325 pm V<sup>-1</sup>, respectively. This piezoelectricity is much stronger than those of the corresponding  $\text{MoA}_2\text{Z}_4$  and  $\text{MoSiGeN}_4$  MLs, attributed to the unique Janus structure of the  $\text{MoAZ}_3\text{H}$  MLs. More importantly, strain can tailor both the spin-valley coupling and piezoelectricity of the  $\text{MoAZ}_3\text{H}$  MLs. Our findings not only enrich the excellent properties of the  $\text{MoAZ}_3\text{H}$  MLs, but also indicate a direction for their application in valleytronics and energy conversion devices.

Received 14th January 2024,  
Accepted 1st March 2024

DOI: 10.1039/d4tc00188e

rsc.li/materials-c

### 1. Introduction

The extreme values of electronic energy in momentum space are referred to as energy valleys in crystals,<sup>1</sup> which gives electrons an additional degree of freedom except for charge and spin, the valley degree of freedom.<sup>2,3</sup> Valleytronic devices based on the valley degree of freedom as information carriers have unique advantages, such as high integration, fast processing speed, low energy consumption, and nonvolatile nature, and have been considered as the development direction of future electronic devices.<sup>4–8</sup> The booming two-dimensional (2D) materials provide an ideal platform for the study of valleytronics. The newly discovered  $\text{MA}_2\text{Z}_4$  ( $\text{M} = \text{Mo, W, V, Nb}$ ,

$\text{Ta, Ti, Zr, Hf or Cr; A = Si or Ge; Z = N, P or As}$ ) monolayer (ML) family,<sup>9</sup> with a septuple-layer structure, is another intriguing family of 2D valleytronic materials<sup>10,11</sup> after the transition metal dichalcogenides (TMDCs) represented by  $\text{MoS}_2$ ,<sup>12,13</sup> which is attributed to their broken inversion symmetry and strong spin-orbital coupling (SOC) effect. Among them, one class of members has a twofold valley degeneracy related by time-reversal symmetry at the  $K$  and  $K'$  points of the hexagonal Brillouin zone, which exhibits extraordinary spin valley-coupling in the two nonequivalent valleys, leading to valley transport characteristics and spin-valley coupling optical selection rules,<sup>14–16</sup> including  $\text{MoSi}_2\text{Z}_4$  ( $\text{Z} = \text{N, P, or As}$ ),  $\text{MSi}_2\text{N}_4$  ( $\text{M} = \text{Hf, Ti, or Zr}$ ),  $\text{WA}_2\text{Z}_4$  ( $\text{A} = \text{Si, or Ge; Z = P, or As}$ ), etc. In addition, when the magnetic moments are out-of-plane, the spontaneous valley polarization can be driven by both the inversion and time-reversal symmetries breaking in magnetic  $\text{VSi}_2\text{N}_4$  and  $\text{VSi}_2\text{P}_4$  MLs.<sup>17,18</sup>

2D Janus materials have garnered increasing attention owing to their unique physical properties arising from the dissimilar types of atoms on each side.<sup>19</sup> The larger thickness makes the  $\text{MA}_2\text{Z}_4$  MLs have an advantage over the other ML materials in constructing Janus structures. Substituting the  $\text{Ge}$  element for the  $\text{Si}$  element in the  $\text{MSi}_2\text{N}_4$  ( $\text{M} = \text{V, Mo, W, Zr, or Hf}$ ) ML can form stable Janus  $\text{MSiGeN}_4$  MLs, which induces tunable electronic properties,<sup>20</sup> efficient photocatalytic

<sup>a</sup> School of Physics and Electronic Information Engineering, Henan Polytechnic University, Jiaozuo 454000, China.  
E-mail: caixiaolin@hpu.edu.cn

<sup>b</sup> Key Laboratory for Special Functional Materials of Ministry of Education, Collaborative Innovation Center of Nano Functional Materials and Applications, School of Material Science and Engineering, Henan University, Kaifeng 475004, China. E-mail: jiayu@henu.edu.cn

<sup>c</sup> International Laboratory for Quantum Functional Materials of Henan, and School of Physics and Microelectronics, Zhengzhou University, Zhengzhou 450001, China

† Electronic supplementary information (ESI) available. See DOI: <https://doi.org/10.1039/d4tc00188e>

properties,<sup>21,22</sup> Rashba splitting,<sup>23,24</sup> and valley and spin properties.<sup>25–27</sup> The Janus ML XYSiN<sub>2</sub> (X = S, Se, or Te; Y = Mo, or Cr) materials have good stability, high mechanical strength and excellent electronic properties,<sup>28,29</sup> and can be constructed by substituting chalcogen X atoms for the SiN<sub>2</sub> layer on either side of the central Mo atoms in the MoSi<sub>2</sub>N<sub>4</sub> MLs. Forming Janus structures breaks the vertical symmetry of the ML materials and thus causes out-of-plane piezoelectric properties, which is exactly required for energy conversion devices. For instance, Guo *et al.* found both in-plane and out-of-plane piezoelectric polarizations in MSiGeN<sub>4</sub> (M = Mo, or W) MLs.<sup>24</sup>

Our group theoretically proposed the Janus MoAZ<sub>3</sub>H (A = Si, or Ge; Z = N, P, or As) ML materials by substituting H atoms for one AZ atomic layer of MoA<sub>2</sub>Z<sub>4</sub> MLs, exhibiting semiconducting nature with high carrier mobility, and excellent photovoltaic and catalytic performances.<sup>30</sup> However, for such a system including both a strong SOC effect and broken inversion symmetry, the valleytronic and piezoelectric characteristics are not uncovered, which is crucial for their application in valleytronics and energy conversion devices. Consequently, this work aims to systematically explore the valleytronic and piezoelectric properties of MoAZ<sub>3</sub>H MLs using first-principles calculations. The calculated results show that the Janus MoAZ<sub>3</sub>H MLs have obvious valleytronic properties, and comparable spin-valley coupling to that of the corresponding MoA<sub>2</sub>Z<sub>4</sub> MLs, in which the valley Hall effects are observed attributed to the non-zero Berry curvatures with opposite signs at the *K* and *K'* points. Also, Janus MoAZ<sub>3</sub>H MLs not only exhibit stronger in-plane piezoelectric response than the corresponding MoA<sub>2</sub>Z<sub>4</sub> MLs, but also have obvious out-of-plane piezoelectric responses induced by the unique Janus structures. Furthermore, strain can tailor both the spin-valley coupling and piezoelectricity of MoAZ<sub>3</sub>H MLs. Our results show that the MoAZ<sub>3</sub>H MLs with the valleytronic and piezoelectric properties coexisting are promising for valleytronic and energy conversion devices in future.

## 2. Computational details

All calculations are performed in the Vienna *ab initio* simulation package (VASP)<sup>31</sup> based on density functional theory (DFT).<sup>32</sup> The exchange correlation potential is described by the generalized gradient approximation (GGA)<sup>33</sup> with the Perdew–Burke–Ernzerhof (PBE) functional. The cut off energy of

the plane wave is set to 500 eV, and the convergence criteria are 10<sup>−5</sup> eV and 0.01 eV Å<sup>−1</sup> for the energy and the force, respectively. The vacuum space is set to 30 Å to avoid adjacent interactions. The 21 × 21 × 1 Monkhorst–Pack *k*-point mesh is used to sample the Brillouin zone. The Heyd–Scuseria–Ernzerhof (HSE)<sup>34</sup> hybrid functional method is used to obtain a more precise band structure. The maximum-localized Wannier function (MLWF) calculated by the WANNIER90<sup>35</sup> package is used to obtain the high-symmetry point Berry curvature, and the Berry curvature of the 2D section is plotted by the VASP-BERRY code.<sup>36</sup> Meanwhile, the spin texture is calculated using VAVSPKIT.<sup>37</sup>

## 3. Results and discussion

Fig. 1 presents the crystal structures of Janus MoAZ<sub>3</sub>H MLs and corresponding high-symmetric path in the Brillouin zone. It is clearly found that the Janus MoAZ<sub>3</sub>H MLs can be obtained by replacing one AZ layer with H atoms in the MoA<sub>2</sub>Z<sub>4</sub> ML, which still maintains the hexagonal lattice structure, with six atomic layers in a queue of H–Z–Mo–Z–A–Z. As the atomic number of the A or Z element increases, both the lattice constants and the thicknesses of the MoAZ<sub>3</sub>H MLs also gradually increase.

### 3.1 Valleytronic properties

In order to unveil the valleytronic properties of the MoAZ<sub>3</sub>H MLs, we firstly plot the projected band structure of atomic contributions using the PBE scheme, as shown in Fig. S1 (ESI†). Distinctly, the conduction band minima (CBMs) of all the six MoAZ<sub>3</sub>H MLs are at the *K* point. Meanwhile, the *K* point is either the valence band maximum (VBM) or the extreme point of the energy for the highest valence band. All the electronic states of the CBMs and the highest valence bands at the *K* points are mainly determined by the Mo atom of the MoAZ<sub>3</sub>H MLs. Further calculated results in Fig. 2 show that the Mo orbital-resolved band structure shows that the CBM is mainly from the Mo-d<sub>z<sup>2</sup></sub> orbital, while the highest valence band at the *K* point is contributed by the Mo-d<sub>x<sup>2</sup>-y<sup>2</sup></sub> and -d<sub>xy</sub> orbitals. As a result of the C<sub>3h</sub> group at *K*/*K'*, the basis functions are chosen as

$|\varphi_c^\tau\rangle = |\text{d}_{z^2}\rangle$  and  $|\varphi_v^\tau\rangle = \sqrt{\frac{1}{2}}(|\text{d}_{x^2-y^2}\rangle + i\tau|\text{d}_{xy}\rangle)$ , where the subscript *c*(*v*) indicates conduction (valence) band, and  $\tau = \pm 1$  is the valley index corresponding to the *K*/*K'* point. When we approximate the SOC term as an intra-atomic contribution and

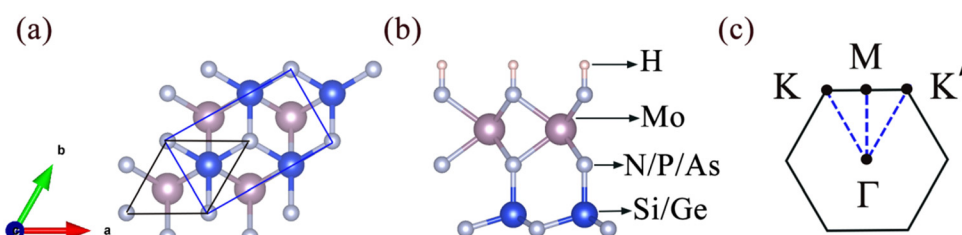


Fig. 1 (a) and (b) are the top and side views of the crystal structures, and (c) the high symmetry path in the Brillouin zone for the MoAZ<sub>3</sub>H MLs, respectively. In panel (a), black rhombi and blue rectangles represent the unit cells and rectangular supercells of the MoAZ<sub>3</sub>H MLs, respectively.

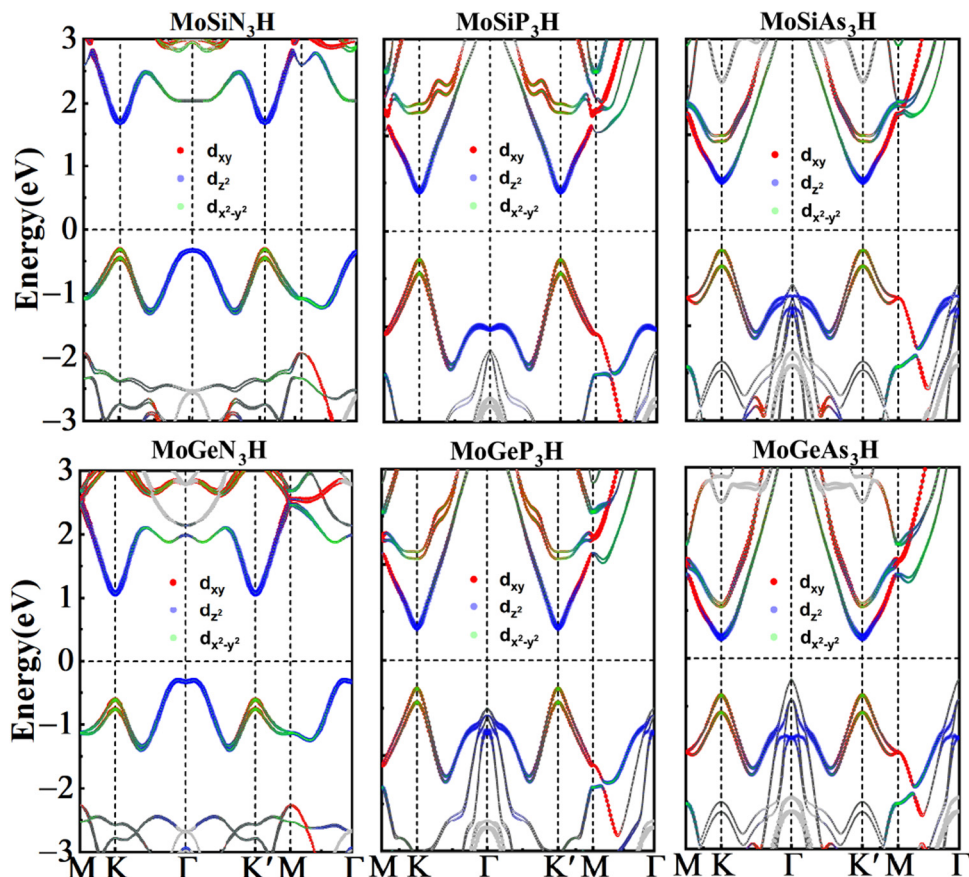


Fig. 2 Orbital-resolved band structures of the d-orbitals of Mo atoms in MoAZ<sub>3</sub>H MLs.

only keep the leading-order term, the  $k\cdot p$  effective model is obtained as

$$\hat{H}^{\tau} = \alpha(\tau k_x \hat{\sigma}_x + k_y \hat{\sigma}_y) + \frac{\Delta}{2} \hat{\sigma}_z - \frac{\lambda}{2} \tau (\hat{\sigma}_z - 1) \hat{\sigma}_z. \quad (1)$$

Here,  $k$  refers to the wave vectors of the  $K$  and  $K'$  points,  $\hat{\sigma}$  refers to the Pauli matrices for the two basis functions, and  $\alpha$  and  $\Delta$  are real-valued model parameters. The third term on the right side of the above equation is the SOC effect term, where  $\hat{\sigma}_z$  is the Pauli matrix for spin and  $\lambda$  is the effective SOC strength. The energies of the VBM and CBM at the  $K/K'$  point are  $E_v^{\tau} = \langle \varphi_v^{\tau} | \hat{H}^{\tau} | \varphi_v^{\tau} \rangle$  and  $E_c^{\tau} = \langle \varphi_c^{\tau} | \hat{H}^{\tau} | \varphi_c^{\tau} \rangle$ . Based on the above analysis, we can obtain the spin splitting of the VBM and CBM at the  $K/K'$  point:

$$\Delta E_v = E_v^- - E_v^+ = i \langle d_{xy} | \hat{H}^{\tau} | d_{x^2-y^2} \rangle - i \langle d_{x^2-y^2} | \hat{H}^{\tau} | d_{xy} \rangle = 2\lambda, \quad (2)$$

$$\Delta E_c = E_c^- - E_c^+ = 0. \quad (3)$$

This result means the significant and negligible spin splittings of the VBM and CBM at the  $K/K'$  point, respectively, which can also be verified by the d-orbital-resolved band structure from the PBE+SOC scheme, as shown in Fig. 2.

Fig. 3 shows the spin-resolved band structures of MoAZ<sub>3</sub>H MLs along the path of  $M-K-\Gamma-K'-M-\Gamma$  using the PBE+SOC method. Firstly, as discussed above, there exists obvious spin

splitting in the band structures of MoAZ<sub>3</sub>H MLs resulting from the strong SOC effect. In particular, due to the broken inversion symmetry as well as the preserved time-reversal symmetry, the highest valence bands at the  $K'$  and  $K$  points have spin polarization in the opposite direction, proving that the Janus MoAZ<sub>3</sub>H MLs have valleytronic properties. These valleytronic properties can also be illustrated by the spin texture for the two highest spin-split valence bands at the  $K/K'$  point over the entire Brillouin zone, and for simplicity, we only calculate the spin texture for MoSiP<sub>3</sub>H and MoGeAs<sub>3</sub>H MLs, as shown in Fig. 4. It is clearly revealed that the out-of-plane components of the spin polarization at the  $K$  and  $K'$  points are opposite at the same band (Fig. 4(a) and (b)); meanwhile, the in-plane components of the spin polarization at the  $K$  or  $K'$  points are also opposite at different bands (Fig. 4(a) and (b)). This fully illustrates the opposite spin polarizations of the highest valence band at the  $K$  and  $K'$  points caused by the strong SOC under the spatial inversion symmetry breaking in Janus MoAZ<sub>3</sub>H MLs.

Table 1 lists the spin-valley coupling ( $\Delta V$ ) and band gap ( $E_g$ ) of MoAZ<sub>3</sub>H MLs both from the PBE+SOC and HSE+SOC schemes. Compared to the PBE+SOC method, although the HSE+SOC method significantly enhances the band gap and spin-valley coupling of the MoAZ<sub>3</sub>H ML (Fig. S2, ESI†), they both predict the same variation trends of the band gap and the

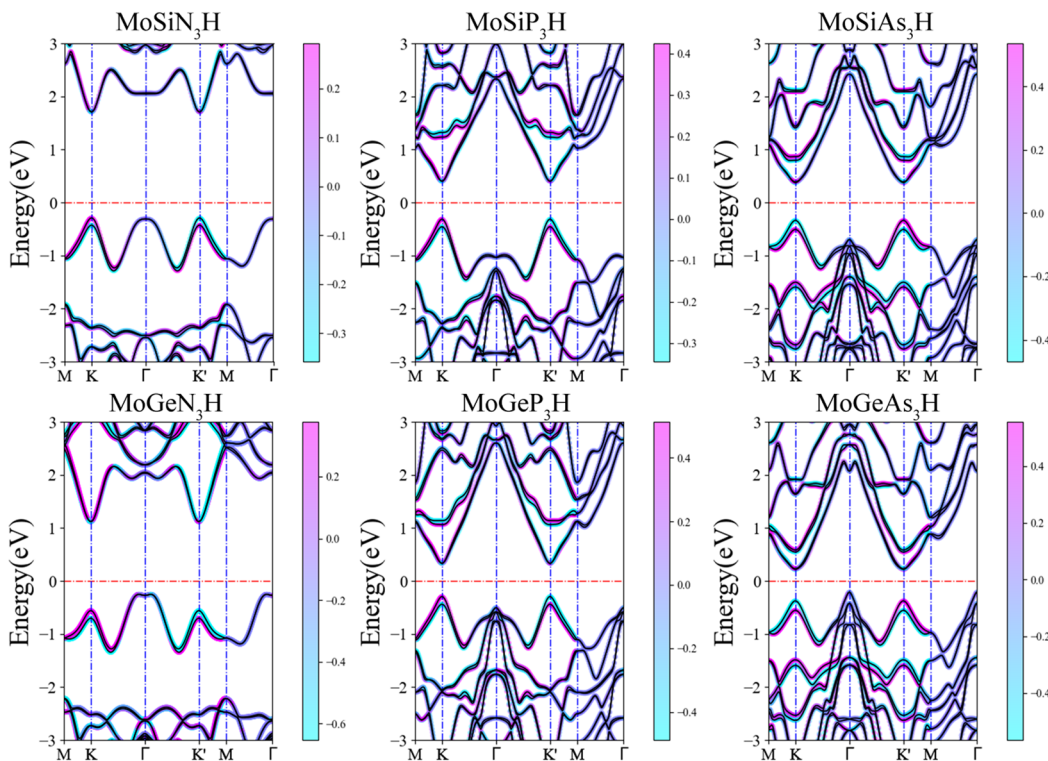


Fig. 3 Spin-resolved band structures of Janus MoAZ<sub>3</sub>H MLs by the PBE+SOC method. Here, the Fermi levels are set to zero.

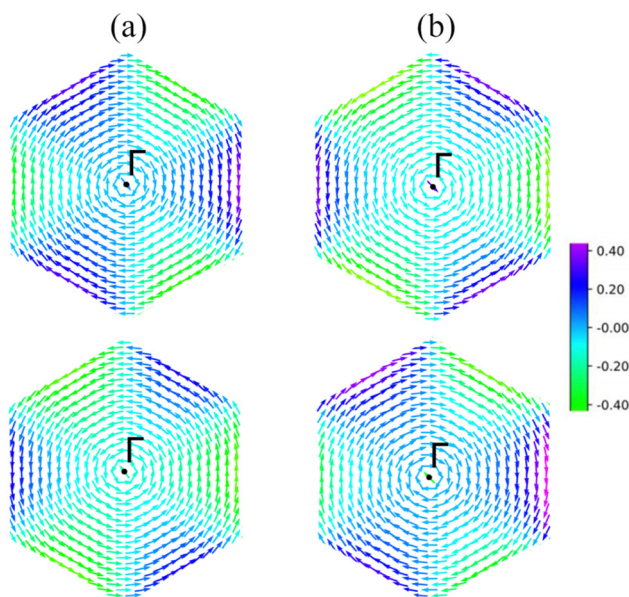


Fig. 4 Spin texture for the two highest spin-split valence bands in (a) MoSiP<sub>3</sub>H and (b) MoGeAs<sub>3</sub>H MLs calculated in the entire BZ, where (a) and (b) include the upper and lower valence bands, respectively. Here, the arrows show the in-plane components of spin polarization, and the colors represent the out-of-plane components of spin polarization.

spin-valley coupling when substituting Ge for Si or substituting P or As for N in the MoAZ<sub>3</sub>H MLs. Among the six members, the

Table 1 Band gap  $E_g$  (eV) and spin-valley coupling  $\Delta V$  (meV) for MoAZ<sub>3</sub>H MLs

	$E_g^{\text{PBE+SOC}}$	$E_g^{\text{HSE+SOC}}$	$E_v^{\text{PBE+SOC}}$	$E_v^{\text{HSE+SOC}}$
MoSiN <sub>3</sub> H	2.00	2.44	136	173
MoSiP <sub>3</sub> H	0.73	0.95	143	203
MoSiAs <sub>3</sub> H	0.69	0.83	172	267
MoGeN <sub>3</sub> H	1.37	1.93	143	184
MoGeP <sub>3</sub> H	0.63	0.78	145	211
MoGeAs <sub>3</sub> H	0.43	0.69	180	283

MoSiN<sub>3</sub>H ML has the smallest spin-valley coupling, about 173 meV, which will increase with both substituting Ge for Si and substituting P or As for N due to the larger radius and mass of the replaced atom. As a result, the largest spin-valley coupling is for MoGeAs<sub>3</sub>H ML, up to 283 meV. It is worth noting that the replacement of the element in Group V has a greater impact on the spin-valley coupling than that in Group IV because there are more atoms with larger mass in Group V in MoAZ<sub>3</sub>H MLs. Previous studies reported that the spin-valley coupling values were 170, 206 and 295 meV for MoSi<sub>2</sub>N<sub>4</sub>, MoSi<sub>2</sub>P<sub>4</sub> and MoSi<sub>2</sub>As<sub>4</sub> MLs,<sup>38</sup> respectively. This means that replacing one SiN or SiP layer with H atoms in the MoSi<sub>2</sub>N<sub>4</sub> ML basically does not change the spin-valley coupling, whereas replacing the SiAs layer with H atoms can slightly reduce the spin-valley coupling due to the lighter replaced atoms.

Unlike the magnetic MLs with the broken time reversal symmetry, such VSi<sub>2</sub>P<sub>4</sub><sup>39</sup> and Mn<sub>2</sub>P<sub>2</sub>X<sub>3</sub>Y<sub>3</sub><sup>40</sup> MLs have spontaneous valley polarization. The valley characteristics of Janus

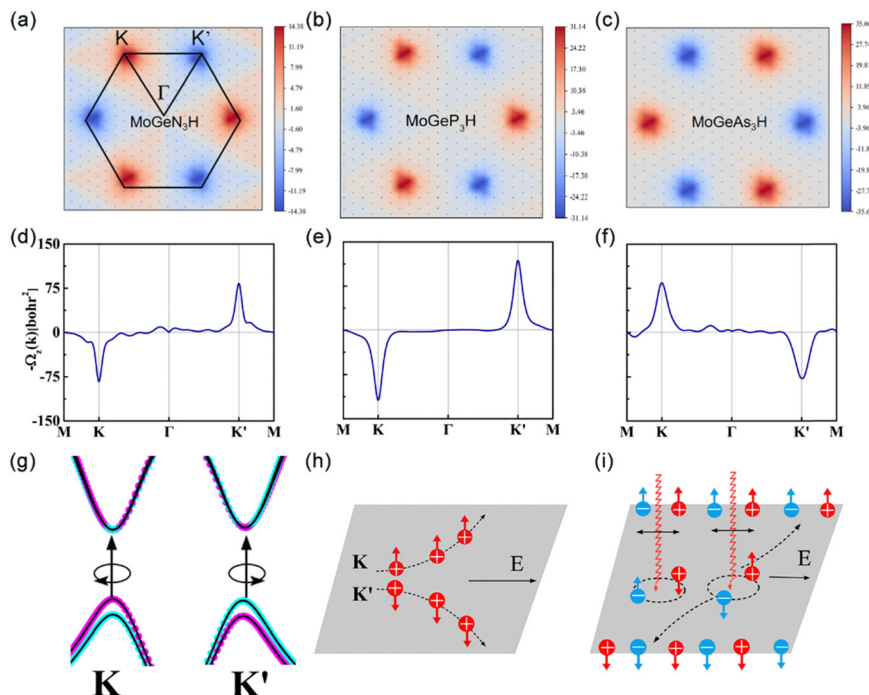


Fig. 5 (a)–(c) are Berry curvature diagrams of Janus MoGeA<sub>3</sub>H (A = N, P, and As) MLs in the Brillouin zone. (d)–(f) are the corresponding Berry curvature curves along the high symmetry path. (g) Spin-resolved valley optical transition selection rules. (h) Schematic diagram of the valley Hall effect for K and K' valleys, where the + sign indicates a hole, and the red up and down arrows represent spin up and down, respectively. (i) Valley Hall effect excited by a linearly polarized optical field.

MoAZ<sub>3</sub>H MLs arise from the spatial inversion symmetry breaking and strong SOC effects, which manifest as spin-valley coupling or opposite spin splitting at the K/K' point, protected by time reversal symmetry. As the atomic number of element A or Z increases, the spin-valley coupling of the MoAZ<sub>3</sub>H MLs ranges from 173 to 283 meV, which is larger than that of the MoS<sub>2</sub> ML (150 meV),<sup>1</sup> while much smaller than those of H-Tl<sub>2</sub>O (610 meV)<sup>41</sup> and HfN<sub>2</sub> (314 meV)<sup>42</sup> because of the stronger SOC of elements Tl and Hf.

To further demonstrate the valleytronic properties of MoAZ<sub>3</sub>H ML, we also calculate the Berry curvatures of MAZ<sub>3</sub>H MLs based on the Kudo formula:<sup>43</sup>

$$\Omega(k) = -2 \sum_n \sum_{n' \neq n} f_n \frac{\text{Im} \langle \psi_{nk} | v_x | \psi_{n'k} \rangle \langle \psi_{n'k} | v_y | \psi_{nk} \rangle}{(E_{n'} - E_n)^2}, \quad (4)$$

where  $f_n$ ,  $E_n$  ( $k$ ), and  $v_{x/y}$  are the Fermi-Dirac distribution function, eigenvalue of the Bloch state  $\psi_{nk}$ , and velocity operator along the x/y directions, respectively. Berry curvatures of MAZ<sub>3</sub>H MLs in the 2D Brillouin zone are presented in Fig. S3(a)–(c) (ESI†) and Fig. 5(a)–(c). As expected, the Berry curvatures at the K and K' valleys exhibit opposite signs for the MAZ<sub>3</sub>H systems, namely  $\Omega(k) = -\Omega(k')$ , which is also verified by the curve of the Berry curvatures of MAZ<sub>3</sub>H MLs along the high symmetry path in Fig. S3(d)–(f) (ESI†) and Fig. 5(d)–(f). The values of Berry curvature at the K and K' valleys are non-zero and of opposite signs, spanning 75–120 bohr<sup>2</sup>, which is further evidence of the valleytronic properties of the MAZ<sub>3</sub>H MLs. Such valley nature gives rise to the valley-contrasting spin splitting,

inducing the spin-dependent valley optical selection rule,<sup>44</sup> as illustrated in Fig. 5(g). Additionally, the non-zero Berry curvature is similar to the effective magnetic field in the presence of an in-plane electric field. Due to the opposite Berry curvatures at the K and K' valleys, the electrons at the K and K' valleys can obtain two anomalous velocities:<sup>45</sup>  $v_n(k) = \frac{\partial \epsilon_n(k)}{\hbar \partial k} - \frac{e}{\hbar} E \times \Omega(k)$ , which are perpendicular to the electric field and move in opposite directions as shown in Fig. 5(h), leading to the valley Hall effect, which can also be excited by a linearly polarized optical field (Fig. 5(i)).

### 3.2 Piezoelectric properties

Next, we turn to explore both in-plane and out-of-plane piezoelectric effects in the MoAZ<sub>3</sub>H MLs with a unique Janus structure. For the 2D ML with P3m1 symmetry, the elastic and piezoelectric tensors be reduced into:<sup>46</sup>

$$C = \begin{pmatrix} C_{11} & C_{12} & 0 \\ C_{12} & C_{11} & 0 \\ 0 & 0 & \frac{C_{11} - C_{12}}{2} \end{pmatrix}, \quad (5)$$

$$e = \begin{pmatrix} e_{11} & -e_{11} & 0 \\ 0 & 0 & -e_{11} \\ e_{31} & e_{31} & 0 \end{pmatrix}, \quad (6)$$

$$d = \begin{pmatrix} d_{11} & -d_{11} & 0 \\ 0 & 0 & -2d_{11} \\ d_{31} & d_{31} & 0 \end{pmatrix}. \quad (7)$$

A uniaxial in-plane strain can induce both the in-plane and out-of-plane piezoelectric responses ( $e_{11}/d_{11} \neq 0$  and  $e_{31}/d_{31} \neq 0$ ), while a biaxial in-plane strain can only produce an out-of-plane piezoelectric response ( $e_{11}/d_{11} = 0$  but  $e_{31}/d_{31} \neq 0$ ). Solving equation  $e_{ik} = d_{ij}C_{jk}$  can derive the independent  $d_{11}$  and  $d_{31}$ :

$$d_{11} = \frac{e_{11}}{C_{11} - C_{12}} \quad \text{and} \quad d_{31} = \frac{e_{31}}{C_{11} + C_{12}}. \quad (8)$$

Piezoelectric stress, strain and elastic tensors of  $\text{MAZ}_3\text{H}$  MLs can be obtained from eqn (5)–(8) using the orthorhombic supercell (Fig. 1(a)), as listed in Table 2. Compared to  $\text{MA}_2\text{Z}_4$  MLs, the Janus  $\text{MAZ}_3\text{H}$  MLs break the reflection symmetry with respect to the central Mo atom due to the two different surface atoms in the vertical direction, leading to the non-zero  $e_{31}/d_{31}$ .

It is firstly found that the piezoelectric coefficients  $e_{11}/e_{31}$  of the  $\text{MoSiN}_3\text{H}$  and  $\text{MoGeN}_3\text{H}$  MLs are about  $4.146/0.290$  and  $4.112/0.267 \text{ } 10^{-10} \text{ C m}^{-1}$ , respectively. Evidently, the two  $e_{11}$  coefficients are comparable to that of  $\text{MoSi}_2\text{N}_4$  ( $\text{MoGe}_2\text{N}_4$ ) ML ( $4.395$  ( $4.218$ )  $10^{-10} \text{ C m}^{-1}$ ), while significantly smaller than that of  $\text{MoSiGeN}_4$  ML ( $5.116 \text{ } 10^{-10} \text{ C m}^{-1}$ ).<sup>24</sup> Apart from the smaller  $e_{11}$  of the  $\text{MoSiAs}_3\text{H}$  ML than that of the  $\text{MoGeAs}_3\text{H}$  ML, the  $\text{MoSiZ}_3\text{H}$  MLs have larger  $e_{11}$  values than the  $\text{MoGeZ}_3\text{H}$  systems. The size order of  $e_{11}$  is  $\text{MoSiP}_3\text{H} > \text{MoSiAs}_3\text{H} > \text{MoSiN}_3\text{H}$  in the  $\text{MoSiZ}_3\text{H}$  MLs, whereas the  $e_{11}$  of the  $\text{MoGeZ}_3\text{H}$  ML increases with the increasing mass of Z element. The maximum  $e_{11}$  is  $7.583 \text{ } 10^{-10} \text{ C m}^{-1}$  for the  $\text{MoSiP}_3\text{H}$  ML. The  $\text{MoSiZ}_3\text{H}$  MLs have a slightly larger  $e_{31}$  than the  $\text{MoGeZ}_3\text{H}$  systems, and the  $e_{31}$  values of the  $\text{MoAN}_3\text{H}$  MLs are slightly larger than those of the  $\text{MoAP}_3\text{H}$  MLs, while much smaller than those of the  $\text{MoAAAs}_3\text{H}$  MLs. In the  $e_{11}/e_{31}$  of  $\text{MoAN}_3\text{H}$  system, the electronic contribution has the opposite sign to the ionic contribution, while the electronic and ionic contributions dominate  $e_{11}$  and  $e_{31}$ , respectively, as shown in Fig. 6(a) and (b), respectively. However, for the  $\text{MoAP}_3\text{H}$  and  $\text{MoAAAs}_3\text{H}$  MLs, the electronic and ionic contributions have the same signs in  $e_{11}/e_{31}$ . This may be why the  $e_{11}/e_{31}$  of the  $\text{MoAN}_3\text{H}$  systems are smaller.

As discussed in previous research,<sup>30</sup> the elastic constant of the  $\text{MoAN}_3\text{H}$  ML is the largest in all of the  $\text{MoAZ}_3\text{H}$  MLs, mostly larger than twice those of the other  $\text{MoAZ}_3\text{H}$  MLs, and the

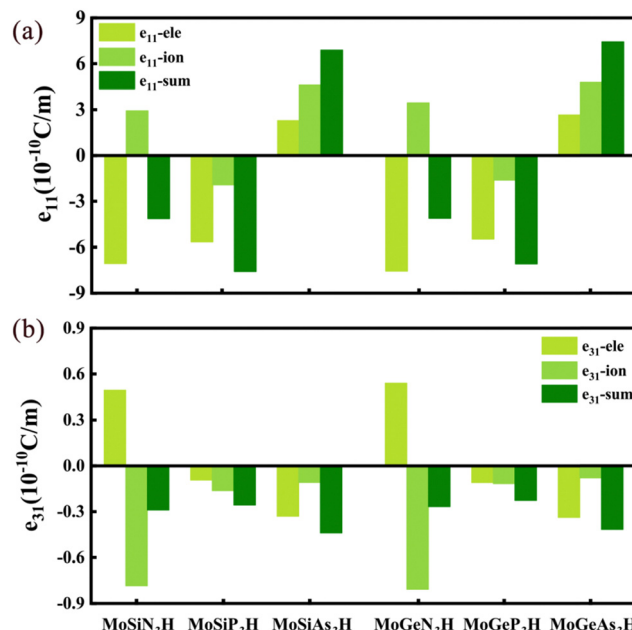


Fig. 6 Ionic and electronic contributions of the piezoelectric coefficients (a)  $e_{11}$  and (b)  $e_{31}$  in the  $\text{MoAZ}_3\text{H}$  ML, respectively.

$\text{MoAP}_3\text{H}$  ML has a slightly larger elastic constant than the  $\text{MoAAAs}_3\text{H}$  ML. Consequently, the values of  $C_{11} + C_{12}$  and  $C_{11} - C_{12}$  are decreasing with increasing atomic mass of A or Z element for the  $\text{MoAZ}_3\text{H}$  ML. The piezoelectric coefficients  $d_{11}/d_{31}$  are  $1.62/0.058 \text{ pm V}^{-1}$  for the  $\text{MoSiN}_3\text{H}$  ML and  $2.32/0.069 \text{ pm V}^{-1}$  for the  $\text{MoGeN}_3\text{H}$  ML, respectively, both much larger than that of the Janus  $\text{MoSiGeN}_4$  ML ( $1.49/0.014 \text{ pm V}^{-1}$ ).<sup>24</sup> In particular, the  $\text{MoSiN}_3\text{H}$  and  $\text{MoGeN}_3\text{H}$  MLs have larger  $d_{11}$  than the  $\text{MoSi}_2\text{N}_4$  ( $1.14 \text{ pm V}^{-1}$ ) and  $\text{MoGe}_2\text{N}_4$  ( $1.05 \text{ pm V}^{-1}$ ) MLs.<sup>24</sup> As the atomic mass of A or Z element increases, the  $d_{11}$  value gets larger mainly because of the decreasing  $C_{11} - C_{12}$ , on which changing the element Z has a greater effect. Hence, the  $\text{MoGeAs}_3\text{H}$  ML has the maximum  $d_{11}$  of  $8.60 \text{ pm V}^{-1}$ . Furthermore, for  $\text{MoAZ}_3\text{H}$  MLs, increasing the atomic mass of Z element can greatly enhance the out-of-plane piezoelectric coefficient  $d_{31}$ , mainly resulting from the decreasing  $C_{11} + C_{12}$ . Increasing the atomic number of the A element can increase the  $d_{31}$  for the  $\text{MoAN}_3\text{H}$  and  $\text{MoAAAs}_3\text{H}$  MLs whereas slightly reduce it for the  $\text{MoAP}_3\text{H}$  ML. The maximum  $d_{31}$  is  $0.325 \text{ pm V}^{-1}$  for the  $\text{MoGeAs}_3\text{H}$  ML.

The above discussion fully demonstrates that for  $\text{MA}_2\text{Z}_4$  MLs, forming  $\text{MoAZ}_3\text{H}$  Janus MLs is beneficial for improving the in-plane piezoelectric response  $d_{11}$  values and also for inducing larger out-of-plane piezoelectric responses, larger than forming  $\text{MoSiGeN}_4$  Janus MLs.

### 3.3 Strain effect

Strain is an effective way to control the electronic properties of 2D materials because they can withstand large strain due to the unique crystal structure.<sup>47</sup> Below, we will investigate the strain effect on the spin-valley coupling and piezoelectric properties of Janus  $\text{MoAZ}_3\text{H}$  MLs. Because this work only focuses on the

Table 2 Elastic constants  $C_{11}/C_{12}$  ( $\text{N m}^{-1}$ ) and piezoelectric coefficients  $e_{11}/e_{31}$  ( $10^{-10} \text{ C m}^{-1}$ ) and  $d_{11}/d_{31}$  ( $\text{pm V}^{-1}$ ) of  $\text{MAZ}_3\text{H}$  MLs

	$C_{11}$	$C_{12}$	$e_{11}$	$d_{11}$	$e_{31}$	$d_{31}$
$\text{MoSiN}_3\text{H}$	375.96	120.89	4.146	1.622	0.290	0.058
$\text{MoSiP}_3\text{H}$	159.70	44.38	7.583	6.576	0.257	0.126
$\text{MoSiAs}_3\text{H}$	130.42	43.16	6.884	7.890	0.440	0.254
$\text{MoGeN}_3\text{H}$	282.03	104.55	4.112	2.317	0.267	0.069
$\text{MoGeP}_3\text{H}$	149.76	46.82	7.080	6.877	0.227	0.115
$\text{MoGeAs}_3\text{H}$	128.56	42.15	7.429	8.598	0.418	0.325
$\text{MoSi}_2\text{N}_4^{24}$	—	—	4.395	1.144	—	—
$\text{MoGe}_2\text{N}_4^{24}$	—	—	4.218	1.050	—	—
$\text{MoSiGeN}_4^{24}$	—	—	5.116	1.494	0.087	0.014

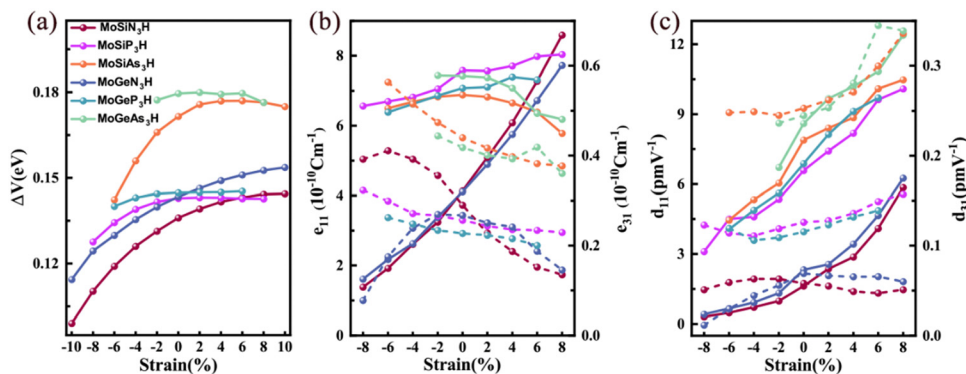


Fig. 7 (a) Spin-valley coupling at the  $K$  point, (b) piezoelectric coefficients  $e_{11}/e_{31}$  and (c)  $d_{11}/d_{31}$  under biaxial strain in the  $\text{MoAZ}_3\text{H}$  MLs. In the three panels, the solid lines in one color and the corresponding dashed lines indicate the results of the same material.

semiconducting characteristics of the  $\text{MoAZ}_3\text{H}$  MLs, it excludes the  $\text{MoAZ}_3\text{H}$  MLs transforming to metals under strain. Table 1 reveals that the increasing atomic number of element A or Z in the  $\text{MoAZ}_3\text{H}$  ML can gradually decrease the band gap, which would also narrow the strain range of maintaining the semiconducting properties. Thus, different strain ranges are considered for the  $\text{MoAZ}_3\text{H}$  MLs with different components. In addition, it was revealed that Janus  $\text{MoAZ}_3\text{H}$  MLs under zero strain exhibit good dynamic stability due to no imaginary frequency in the phonon spectra.<sup>30</sup> We also calculate the phonon spectra of strained  $\text{MoAZ}_3\text{H}$  MLs, and find that the phonon spectra have no imaginary frequency under the considered tensile strain and are prone to showing imaginary frequencies under large compressive strain. Fig. S4 (ESI<sup>†</sup>) presents the phonon spectra of the  $\text{MoSiN}_3\text{H}$ ,  $\text{MoSiAs}_3\text{H}$  and  $\text{MoGeN}_3\text{H}$  MLs under the tensile strain of 10%, in which there are no imaginary frequencies. This means that  $\text{MoAZ}_3\text{H}$  MLs can sustain a larger tensile strain, whereas the compressive stress has a greater destructive force on the systems.

Fig. 7(a) shows the strain tunable spin-valley coupling of the highest valence bands at the  $K/K'$  points of  $\text{MoAZ}_3\text{H}$  MLs. There is little change in the spin-valley couplings of the  $\text{MoGeAs}_3\text{H}$  and  $\text{MoGeP}_3\text{H}$  MLs under strain. Besides, for the other four  $\text{MoAZ}_3\text{H}$  MLs, the spin-valley coupling is enhanced by the tensile strain, while weakened by the compressive strain, which indicates that strain can easily regulate spin-valley coupling strength, having potential applications in valleytronic devices. Fig. 7(b) and (c) present the responses of the piezoelectric coefficients to strain for the  $\text{MoAZ}_3\text{H}$  MLs, which obviously illustrates that the piezoelectric coefficients can be easily tailored by strain. Overall, among the four piezoelectric coefficients, the most strain-regulated is  $d_{11}$ , which basically increases and decreases with increasing tensile and compressive strains, respectively. The same strain regulation rule is followed by the  $e_{11}$  of the  $\text{MoAN}_3\text{H}$  and  $\text{MoAP}_3\text{H}$  MLs, whereas that of the  $\text{MoAN}_3\text{H}$  MLs changes more significantly with strain. The  $e_{11}$  of the  $\text{MoSiAs}_3\text{H}$  ML always reduces with both tensile and compressive strains, and that of the  $\text{MoGeAs}_3\text{H}$  ML gradually decreases with strain from  $-2\%$  to  $8\%$ . The  $e_{31}$  of the  $\text{MoSiN}_3\text{H}$  ML gradually decreases with increasing tensile strain,

and increases with increasing compressive strain until it reaches  $-6\%$  and then decreases. For the  $\text{MoGeN}_3\text{H}$  ML, the  $e_{31}$  has a maximum under the strain of  $-2\%$ , decreasing with the strain from  $-2\%$  to  $8\%$ . For the  $\text{MoAP}_3\text{H}$  and  $\text{MoAAAs}_3\text{H}$  MLs, the  $e_{31}$  increases and decreases with the compressive and tensile strains, respectively, while the  $d_{31}$  is the opposite. In addition, the fluctuation range of  $d_{31}$  under strain for the six  $\text{MoAZ}_3\text{H}$  MLs is not too large.

It is worth emphasizing that for the  $\text{MoZ}_2$  MLs with poor stability, the H atoms or the AZ layer passivating can make the system more stable.<sup>48,49</sup> More importantly, this means that this can transform the system into a semiconductor with valleytronic characteristics. Thus, we propose to construct stable Janus  $\text{MoAZ}_3\text{H}$  MLs by passivating the two surface Z atoms of  $\text{MoZ}_2$  MLs with one AZ layer and one H atomic layer, respectively, which endows the systems with the unique nature induced by asymmetry of the surface atoms other than the semiconducting and valley properties, such as photovoltaic properties and piezoelectricity.

## 4. Conclusions

To sum up, using first-principles calculations, we find that valleytronic and piezoelectric properties coexist in Janus  $\text{MoAZ}_3\text{H}$  ML materials. The unique valleytronic properties arise from broken inversion symmetry and strong SOC effects, which brings about non-zero Berry curvatures with opposite signs at the  $K$  and  $K'$  valleys and the valley Hall effects. In addition, the in-plane piezoelectric responses of Janus  $\text{MoAZ}_3\text{H}$  MLs are stronger than those of the corresponding  $\text{MoA}_2\text{Z}_4$  MLs. Surprisingly, the unique Janus structure induces obvious out-of-plane piezoelectric responses, and the out-of-plane piezoelectric coefficients  $e_{31}/d_{31}$  are high up to  $0.418 \times 10^{-10} \text{ C m}^{-1}/0.325 \text{ pm V}^{-1}$ . More importantly, strain can tailor both the spin-valley coupling and piezoelectricity of  $\text{MoAZ}_3\text{H}$  MLs. The coexisting valleytronic and piezoelectric properties win a wide application space in the valleytronics and energy conversion fields for the  $\text{MoAZ}_3\text{H}$  MLs.

## Conflicts of interest

There are no conflicts of interest to declare.

## Acknowledgements

This work was supported partly by the National Natural Science Foundation of China (Grant No. 11804082, 12074102 and 11774078), and by the Doctoral Foundation of Henan Polytechnic University (B2018-37). All the calculations were carried out at the Center for High Performance Computing of Henan Polytechnic University.

## References

- 1 D. Xiao, G.-B. Liu, W. Feng, X. Xu and W. Yao, *Phys. Rev. Lett.*, 2012, **108**(19), 196802.
- 2 A. H. Castro Neto, F. Guinea, N. M. R. Peres, K. S. Novoselov and A. K. Geim, *Rev. Mod. Phys.*, 2009, **81**, 109–162.
- 3 J. R. Schaibley, H. Yu, G. Clark, P. Rivera, J. S. Ross, K. L. Seyler, W. Yao and X. Xu, *Nat. Rev. Mater.*, 2016, **1**, 16055.
- 4 B. Urbaszek and X. Marie, *Nat. Phys.*, 2015, **11**, 94–95.
- 5 F. Amet and G. Finkelstein, *Nat. Phys.*, 2015, **11**, 989–990.
- 6 X. Li and G. Moody, *Nat. Phys.*, 2017, **13**, 9–10.
- 7 H. Yu and W. Yao, *Nat. Mater.*, 2017, **16**, 876–877.
- 8 F. Zhang, *Nat. Phys.*, 2018, **14**, 111–113.
- 9 L. Cao, G. Zhou, Q. Wang, L. K. Ang and Y. S. Ang, *Appl. Phys. Lett.*, 2021, **118**, 013116.
- 10 B. Liu, *Natl. Sci. Rev.*, 2020, **7**, 1841–1842.
- 11 S. Li, W. Wu, X. Feng, S. Guan, W. Feng, Y. Yao and S. Yang, *Phys. Rev. B*, 2020, **102**, 235435.
- 12 K. Mak, C. Lee, J. Hone, J. Shan and T. Heinz, *Phys. Rev. Lett.*, 2010, **105**, 136805.
- 13 K. F. Mak, K. L. McGill, J. Park and P. L. McEuen, *Science*, 2014, **344**, 1489–1492.
- 14 Y. Shao, Y. Fang, T. Li, Q. Wang, Q. Dong, Y. Deng, Y. Yuan, H. Wei, M. Wang, A. Gruverman, J. Shield and J. Huang, *Energy Environ. Sci.*, 2016, **9**, 1752–1759.
- 15 C. Yang, Z. Song, X. Sun and J. Lu, *Phys. Rev. B*, 2021, **103**, 035308.
- 16 J.-S. Yang, L. Zhao, S.-Q. Li, H. Liu, L. Wang, M. Chen, J. Gao and J. Zhao, *Nanoscale*, 2021, **13**, 5479–5488.
- 17 X. Y. Feng, X. L. Xu, Z. L. He, R. Peng, Y. Dai, B. B. Huang and Y. D. Ma, *Phys. Rev. B*, 2021, **104**, 075421.
- 18 Q. R. Cui, Y. M. Zhu, J. H. Liang, P. Cui and H. X. Yang, *Phys. Rev. B*, 2021, **103**, 085421.
- 19 Y. Duan, X. Zhao, M. Sun and H. Hao, *Ind. Eng. Chem. Res.*, 2021, **60**, 1071–1095.
- 20 V. T. T. Vi, T. P. T. Linh, C. Q. Nguyen and N. N. Hieu, *Adv. Theory Simul.*, 2022, **5**, 2200499.
- 21 Y. Yu, J. Zhou, Z. Guo and Z. Sun, *ACS Appl. Mater. Interfaces*, 2021, **13**, 28090–28097.
- 22 M.-Y. Liu, Y. He, X. Li and K. Xiong, *Phys. Chem. Chem. Phys.*, 2023, **25**, 7278–7288.
- 23 L. Wu, W. Zhou, D. Zhang and F. Ouyang, *J. Phys.: Conf. Ser.*, 2022, **2263**, 012014.
- 24 S.-D. Guo, W.-Q. Mu, Y.-T. Zhu, R.-Y. Han and W.-C. Ren, *J. Mater. Chem. C*, 2021, **9**, 2464–2473.
- 25 S. Sheoran, A. Phutela, R. Moulik and S. Bhattacharya, *J. Phys. Chem. C*, 2023, **127**, 11396–11406.
- 26 S.-D. Guo, W.-Q. Mu, J.-H. Wang, Y.-X. Yang, B. Wang and Y.-S. Ang, *Phys. Rev. B*, 2022, **106**, 064416.
- 27 Y. Li, M. Lan, S. Wang, T. Huang, Y. Chen, H. Wu, F. Li and Y. Pu, *Phys. Chem. Chem. Phys.*, 2023, **25**, 15676–15682.
- 28 R. T. Sibatov, R. M. Meftakhutdinov and A. I. Kochaev, *Appl. Surf. Sci.*, 2022, **585**, 152465.
- 29 P. T. L. Tran, N. V. Hieu, H. Bui D, Q. N. Cuong and N. N. Hieu, *Nanoscale Adv.*, 2023, **5**, 3104–3113.
- 30 X. Cai, G. Chen, R. Li, W. Yu, X. Yang and Y. Jia, *Phys. Chem. Chem. Phys.*, 2023, **25**, 29594–29602.
- 31 G. Kresse and J. Hafner, *Phys. Rev. B: Condens. Matter Mater. Phys.*, 1993, **47**, 558–561.
- 32 P. Hohenberg and W. Kohn, *Phys. Rev.*, 1964, **136**, B864–B871.
- 33 J. P. Perdew, K. Burke and M. Ernzerhof, *Phys. Rev. Lett.*, 1996, **77**, 3865–3868.
- 34 J. Heyd, G. E. Scuseria and M. Ernzerhof, *J. Chem. Phys.*, 2003, **118**, 8207–8215.
- 35 N. Marzari, A. A. Mostofi, J. R. Yates, I. Souza and D. Vanderbilt, *Rev. Mod. Phys.*, 2012, **84**, 1419–1475.
- 36 T. Fukui, Y. Hatsugai and H. Suzuki, *J. Phys. Soc. Japan.*, 2005, **74**, 1674–1677.
- 37 V. Wang, N. Xu, J.-C. Liu, G. Tang and W.-T. Geng, *Comput. Phys. Commun.*, 2021, **267**, 108033.
- 38 H. Ai, D. Liu, J. Geng, S. Wang, K. H. Lo and H. Pan, *Phys. Chem. Chem. Phys.*, 2021, **23**, 3144–3151.
- 39 X. Feng, X. Xu, Z. He, R. Peng, Y. Dai, B. Huang and Y. Ma, *Phys. Rev. B*, 2021, **104**, 075421.
- 40 Y. Xu, H. Liu, Y. Dai, B. Huang and W. Wei, *Appl. Phys. Lett.*, 2023, **122**, 242404.
- 41 Y. Ma, L. Kou, A. Du, B. Huang, Y. Dai and T. Heine, *Phys. Rev. B*, 2018, **97**, 035444.
- 42 M. K. Mohanta and A. De Sarkar, *Phys. Rev. B*, 2020, **102**, 125414.
- 43 D. J. Thouless, M. Kohmoto, M. P. Nightingale and M. den Nijs, *Phys. Rev. Lett.*, 1982, **49**, 405–408.
- 44 D. Xiao, G.-B. Liu, W. Feng, X. Xu and W. Yao, *Phys. Rev. Lett.*, 2012, **108**, 196802.
- 45 D. Xiao, M.-C. Chang and Q. Niu, *Rev. Mod. Phys.*, 2010, **82**, 1959–2007.
- 46 M. Blonsky, H. L. Zhuang, A. K. Singh and R. G. Hennig, *ACS Nano*, 2015, **9**(10), 9885–9891.
- 47 X. H. Peng, Q. Wei and A. Copple, *Phys. Rev. B: Condens. Matter Mater. Phys.*, 2014, **90**, 085402.
- 48 J. Yuan, Q. Wei, M. Sun, X. Yan, Y. Cai, L. Shen and U. Schwingenschlgl, *Phys. Rev. B*, 2022, **105**, 195151.
- 49 Y. Wang and Y. Ding, *J. Mater. Chem. C*, 2016, **4**, 7485–7493.